Journal of Power Sources 196 (2011) 5240–5249

Contents lists available at ScienceDirect

Journal of Power Sources

journal homepage: www.elsevier.com/locate/jpowsour

Activity of dealloyed $PtCo_3$ and $PtCu_3$ nanoparticle electrocatalyst for oxygen reduction reaction in polymer electrolyte membrane fuel cell

Mehtap Oezaslan[a,*], Peter Strasser[a,b]

[a] The Electrochemical Energy, Catalysis, and Materials Science Laboratory, Department of Chemistry, Chemical Engineering Division, Technical University Berlin, Sekr. TC03, Strasse des 17, Juni 124, 10623 Berlin, Germany
[b] Ertl Center for Electrochemistry and Catalysis, Gwangju Institute of Science and Technology (GIST), Gwanju 500-712, South Korea

ARTICLE INFO

Article history:
Received 20 August 2010
Received in revised form 28 October 2010
Accepted 3 November 2010
Available online 11 November 2010

Keywords:
$PtCo_3$
$PtCu_3$
Electrocatalyst
Oxygen reduction reaction ORR
H_2O_2 production

ABSTRACT

We report a comparative study of the alloy formation and electrochemical activity of dealloyed $PtCo_3$ and $PtCu_3$ nanoparticle electrocatalysts for the oxygen reduction reaction (ORR). For the Pt–Co system the maximum annealing temperatures were 650 °C, 800 °C and 900 °C for 7 h to drive the Pt–Co alloy formation and the particle growth. EDS and XRD were employed for the characterization of catalyst powders. The RDE and RRDE experiments were conducted in 0.1 M $HClO_4$ at room temperature.

We demonstrate that the mass and surface area specific ORR activities of Pt–Co and Pt–Cu alloys after voltammetric activation exhibit a considerable improvement compared to those of pure Pt/C. The dealloyed $PtCo_3$ (800 °C/7 h) electrocatalyst performs 3 times higher in terms of Pt-based mass activity and 4–5 times higher in terms of ECSA-based specific activity than a 28.2 wt.% Pt/C. Dealloyed Pt–Co catalysts (800 °C/7 h) show the most favorable balance between mass and specific ORR activity with a particle size of 2.2 ± 0.1 nm. We hypothesize that geometric strain effects of the dealloyed Pt–Co nanoparticles, similar to those found in dealloyed $PtCu_3$ nanoparticles, are responsible for the improvement in ORR activity [1].

1. Introduction

The polymer electrolyte membrane fuel cell (PEMFC), a device that converts chemical energy directly into electrical energy, is one of the promising applications to solve the challenging problems related to a clean energy production and conversion. Currently, the most widely used electrocatalyst for PEMFC consists of carbon-supported platinum nanoparticles. But, the critical issues should be addressed: the less catalytic efficiency for the oxygen reduction reaction (ORR) ($O_2 + 4H^+ + 4e^- \rightarrow 2H_2O$), the high material cost and the Pt degradation, such as Pt dissolution, Ostwald ripening, coalescence, carbon corrosion and Pt detachment. Under the operating conditions the kinetic limitation of ORR causes to a cathodic overpotential loss of around 0.3–0.4 V, associating with the surface adsorption and the reductive charge transfer process on the catalyst surface [2]. The research of new efficient electrocatalysts with a considerable performance for ORR superior of that of pure platinum is the main effort during the last decade. Recently, Pt alloys with transition metals (PtM with M = Fe, Co, Cu, Ni, etc.) have arrested large attention for the commercial implementation of PEMFC due to the increasing improvement for the ORR performance, the resistance to sintering and coalescence of nanoparticles and the decrease of the Pt loading and the material cost [3–11]. The significantly improved ORR activity of Pt alloy nanoparticles is attributed to many influences such as electronic effects (ligand effect), ensemble effect, geometric effect (Pt–Pt interatomic distance), particle size effect and surface roughness (facets and steps) [8,12–18].

In particular, Pt–Co alloy nanoparticles are very interesting as cathodic electrocatalysts in PEMFC, due to the significantly increasing improvement for intrinsic ORR activity [4,8,19–31]. Recently, we presented a study of dealloyed PtM_3 (M = Co, Cu, Ni) electrocatalysts in a real operating condition of a single fuel cell test station [32]. The membrane electrode assemblies of dealloyed $PtCo_3$ and $PtCu_3$ catalysts show a considerable performance for ORR compared to pure Pt/C. However, the synthesis of $PtCo_3$ nanoparticles need more works to understand and optimize the uniformity of the Pt–Co alloy phase structure with small particle size. We also reported the formation of a voltammetric pretreated Pt rich shell–Cu rich alloy core nanoparticle and particularly the compressive lattice strain in the Pt rich surface layers using microscopic and spectroscopic techniques. The presence of the compressive lattice strain in the Pt shell of a dealloyed nanoparticle related with the significantly enhanced activity. Based on the compressive Pt–Pt distance of the surface atoms the modified d-band structure is weakened for the adsorption energy of reactive intermediates compared to unstrained Pt bulk, which leads to increase in the activity for ORR [1].

* Corresponding author. Tel.: +49 30 314 27883; fax: +49 30 314 22261.
E-mail address: mehtap.oezaslan@tu-berlin.de (M. Oezaslan).

0378-7753/$ – see front matter.
doi:10.1016/j.jpowsour.2010.11.016

In this paper, we present a comparative study of the alloy formation and electrochemical activity of dealloyed $PtCo_3$ and $PtCu_3$ nanoparticle electrocatalysts for ORR. The synthesis of $PtCo_3$ was carried out at various maximum annealing temperatures (650 °C, 800 °C and 900 °C) for 7 h to induce Pt–Co alloy alloy formation, structure and particle growth. $PtCo_3$ alloy nanoparticle electrocatalysts were characterized and tested for ORR using XRD, EDS, RDE and RRDE methods and compared with a dealloyed $PtCu_3$ catalyst and a commercial 28.2 wt.% Pt/HSAC. For $PtCo_3$, we provide a structure-reactivity relationship for oxygen reduction in dependence on the annealing temperature. We show that the uniformity of the crystal phase for the alloy catalyst with small particle is essential to understand the ORR kinetic results.

2. Experimental

2.1. Synthesis of $PtCo_3$ and $PtCu_3$ alloy electrocatalysts

$PtCo_3$ and $PtCu_3$ alloy electrocatalysts were synthesized using a liquid metal precursor impregnation method, followed by freeze drying and thermal annealing in a reductive atmosphere. Additionally, $PtCo_3$ nanoparticle catalysts were treated thermal at 650 °C, 800 °C and 900 °C to study the influence of the annealing temperature on the Pt–Co alloy formation, crystal structure and particle growth.

A commercial 28.2 wt.% Pt nanoparticles supported on a high surface area carbon (HSAC) (part no. TEC10E30E, supplied by TKK, Japan) was prepared by adding of a solid $Co(NO_3)_2{\cdot}6H_2O$ (Alfa Aesar, #010694) and $Cu(NO_3)_2{\cdot}2.5H_2O$ (Sigma–Aldrich, #467855) precursor salt to obtain an atomic ratio Pt:M from 1:3 for the alloy electrocatalyst. The precursor salt was then dissolved in deionized water. The suspension was ultrasonicated for 5 min to form thick slurry. The well-dispersed slurry was subsequently frozen in liquid nitrogen for 15 min and freeze-dried in vacuum for few days. The dried fine powder thus formed was thermally annealed at a maximum temperature for 7 h in a reductive atmosphere (4 vol.% H_2/96 vol.% Ar, with a flux of 100 ml min^{-1}, quality of 5.0, supplied by AirLiquid). For the synthesis of Pt–Co and Pt–Cu alloy nanoparticles the temperature program started with 2 h at 250 °C for precursor decomposition followed by 7 h at a maximum temperature for the alloy formation with a heating rate of 10 K min^{-1}. The impact of the Pt–Co alloy formation was studied through the various annealing temperatures at 650 °C, 800 °C and 900 °C for 7 h. By simply opening the furnace, a slow cooling process was achieved by natural convection. The alloy catalyst powder was subsequently gassed with 1 vol.% O_2/99 vol.% N_2 (quality of 5.0, supplied by AirLiquid) at room temperature for 2 h to prevent the carbon burning. The resulting Pt–Co and Pt–Cu alloy catalysts are in a range from 22 wt.% platinum.

All chemicals had not been previously pretreated and stored according to manufacturer's data from the delivery companies.

Energy-dispersive X-ray spectroscopy (EDS) and X-ray diffraction (XRD) were employed to determine the actual stoichiometric bulk composition, the particle size and the crystal structure of $PtCo_3$ and $PtCu_3$ catalyst powders.

2.2. Thin-film preparation on a glassy carbon electrode

For the thin-film preparation about 5 mg of the synthesized $PtCo_3$ or $PtCu_3$ alloy catalyst powder was mixed in 3.98 ml deionized water, 1.00 ml isopropanol and 20 μl 5 wt.% Nafion solution. The catalyst ink was ultrasonicated for 15 min. From the resulting suspension, 10 μl of aliquot was pipetted onto a commercial highly polished, cleaned glassy carbon surface (GC) with a 5 mm diameter of a rotating disk electrode (RDE) and rotating ring disk electrode (RRDE) with outermost pure Pt ring (supplied by PINE, USA). The prepared electrode was subsequently dried at 60 °C for 10 min in air, resulted in a thin, homogenous film of the catalyst on the glassy carbon surface as working electrode. The final catalyst film obtained a typical Pt loading from about 10–14 μg cm_{geo}^{-2}. A commercial 28.2 wt.% Pt/HSAC (part no. TEC10E30E, supplied by TKK, Japan) was taken for the comparison of mass and surface area specific activity for the oxygen reduction reaction (ORR) and platinum electrochemical active surface area (ECSA).

2.3. Electrochemical measurements of the thin catalyst film

For the electrochemical measurements of the thin catalyst film a rotating disk electrode (RDE) and rotating ring disk electrode (RRDE) techniques with a home-made, three-compartment glass cell were employed. Pt gauze was used as counter electrode and the reference electrode was a mercury–mercury sulfate electrode (Princeton Applied Research, AMETEK), which was held in place by a Haber–Luggin capillary. The electrolyte was a 0.1 M $HClO_4$ solution prepared by diluting of 70% redistilled $HClO_4$ (Sigma–Aldrich, #311421) with de-ionized water (18 MOhm at room temperature). All measurements were operated at room temperature. A commercial bipotentiostat (VSP-5, Biologic, France) and a PINE rotator were used to conduct the rotating disk electrode (RDE) and the rotating ring disk electrode (RRDE) experiments. The immersion of the working electrode was occurred under potential control at 0.06 V/RHE until actual measurement commenced. All given potentials were converted and reported in the reversible hydrogen electrode (RHE) scale.

Cyclic voltammetry (CV) was recorded in a potential range between 0.06 and 1.00 V/RHE in deaerated 0.1 M $HClO_4$ electrolyte in a nitrogen atmosphere at room temperature. The dealloying protocol started with three initial CV scans and a scan rate of 100 mV s^{-1}, followed with very fast 200 CV scans and a scan rate of 500 mV s^{-1} and finally three CV scans with a scan rate of 100 mV s^{-1}. The voltammetric response of the electrocatalytic film in the first CV profiles showed a slow surface dissolution of the less noble metal. The electrochemical treatment with 200 CVs and 500 mV s^{-1} affected subsequently the dissolution of a large amount of the less noble metal on the particle surface. The final CV profiles with a scan rate of 100 mV s^{-1} were used to establish the platinum electrochemical active surface area (ECSA) of the dealloyed nanoparticle catalyst. The ECSA was determined using the mean integral charge of the hydrogen adsorption and desorption area with double layer current corrected at 0.40 V/RHE and using 210 μC cm^{-2} (Pt) with an assumption, that one H atom observed to one Pt atom.

ORR activity of voltammetric pretreated catalysts was established through linear sweep voltammetry (LSV) experiment. A 0.1 M $HClO_4$ electrolyte solution was saturated with oxygen by bubbling through a glass fit at room temperature. The LSV experiment was conducted by potential sweeping from 0.06 V/RHE anodically to the open circuit potential (around 1.05 V/RHE) at a scan rate of 5 mV s^{-1} and a rotation speed of 1600 rpm. Polarization curves with various rotating speeds were performed for the Koutecki–Levich plot in oxygen saturated electrolyte at room temperature. Mass and surface area specific activities for ORR were established at 0.90 V/RHE and corrected for mass transport limitation. The peroxide detection and its quantification were found out by measuring the Pt ring current in the RRDE experiment. During the measurements of polarization curves for ORR on the disk electrode, the ring electrode was potentiostated at 1.20 V/RHE. The peroxide oxidation reaction is under diffusion control. The collection efficiency N is around 0.16 ± 0.02. It was determined separately for each rotating speed using the ferrocyanide test. The ring background current was subtracted from the measured ring current, respectively.

2.4. X-ray diffraction

The characterization of the crystal phase structure and particle size of synthesized $PtCo_3$ and $PtCu_3$ catalyst powders was carried out with X-ray diffraction (XRD). The XRD patterns were collected by D8 Advanced X-ray Diffractometer (Bruker AXS) in Bragg-Brentano geometry using a Cu Kα source and a position sensitive LynxEye detector (PSD). 2θ diffraction range was from 15° to 80° with a step size of 0.01°, holding time of 7 s per step, variable divergence slit of 4 mm, PSD Iris from 13 and with a sample rotation of 15 rpm. A NIST corundum standard was used for the verification of the instrument resolution. A custom made XRD sample holder with a centered 1 mm depth and 10 mm diameter was filled with the catalyst powder sample. The catalyst powder was given into the well of the sample holder and carefully flattened and flushed to form a smooth surface. All XRD diffraction profiles were analyzed with using Diffrac^{plus} Evolution Package EVA (Bruker AXS, Version 14) and TOPAS (Bruker AXS, Version 4-2). The quantification of crystal phases was established through Rietveld refinement method via TOPAS with the followed parameters: background coefficients, displacement correction, peak shape and cell parameters. The residual values of the refinement, R - weighted pattern (R_{wp}), R - expected (R_{exp}) and the goodness-of-fit (GOF) were subsequently evaluated.

The stoichiometric composition of the crystal phase structure of Pt–Co and Pt–Cu alloy was related with Vegard's law. Vegard's law describes the directly linear dependency on the lattice parameter of the alloy and those single components. The volume averaged crystallite size of alloy nanoparticle catalysts was determined with the integral breadth method via TOPAS, which is independent of the distribution in size and shape.

2.5. Energy-dispersive X-ray spectroscopy

The nominal chemical composition of $PtCo_3$ and $PtCu_3$ alloy nanoparticle catalysts was determined with a high-resolution Hitachi S-4000 Scanning Electron Microscope equipped with a cold field emitter and an energy-dispersive X-ray spectroscope (EDS). The EDS measurements were conducted at an accelerating voltage of 20 kV, a beam current of 0.4 nA and a working distance of 20 mm. The synthesized and voltammetric treated alloy catalyst samples were prepared on carbon tabs (supplied by PLANO, Germany). The sample composition was analyzed and averaged about a large range on different positions. For the quantification the following characteristic peaks were used Kα for Co and Cu and Mα for Pt. The experimental precision is about 2–3 at.%.

3. Results and discussion

3.1. Structural characterization of $PtCo_3$ and $PtCu_3$ electrocatalysts

The bulk composition of $PtCo_3$ (650 °C/7 h), $PtCo_3$ (800 °C/7 h), $PtCo_3$ (900 °C/7 h) and $PtCu_3$ (800 °C/7 h) electrocatalysts obtained from EDS analysis is presented in Table 2. The EDS results reveal that the actual atomic ratio of Pt:M (M = Cu, Co) is close to the nominal 25:75 for all alloys.

Fig. 1 shows the collected X-ray diffraction patterns of Pt–Co and Pt–Cu alloy electrocatalysts supported on high surface area carbon (HSAC). The vertical dotted lines denote the pure Pt, Co and Cu reference patterns with Fm-3m space groups. For the Pt–Co system the maximum annealing temperatures were 650 °C, 800 °C and 900 °C at an annealing time of 7 h to drive the Pt–Co alloy formation and the particle growth. It is clearly observed, that the XRD patterns of the alloys exhibit multiple cubic crystal phase structures. The absence of additional superlattice reflections of the ordered Pt–Co alloy phase structures signifies that all Pt–Co catalysts show a disordered face-centered cubic (fcc) lattice type structure with space group Fm-3m. Crystalline cobalt and platinum were not observed in the XRD profiles. For all samples the reflections of the disordered Pt–Co relate to the diffraction from (1 1 1), (2 0 0) and (2 2 0) lattice planes of the fcc crystal structure with Fm-3m. The (1 1 1), (2 0 0) and (2 2 0) reflections of each disordered Pt–Co sample shifted to higher 2θ angles with respect to pure Pt, indicated the contraction of the lattice and the alloy formation after the thermal treatment at 650 °C, 800 °C and 900 °C for 7 h. For all Pt–Co alloy catalysts, Table 1 presents the results of crystal phase, lattice parameter, crystallite size, Rietveld quantification and stoichiometric alloy composition using Vegard's Law. The XRD peaks of Pt–Co sample (650 °C/7 h) show a sight additional left shoulder, signifying probably a third minor fraction with lower degree of the alloy. The main compound of the disordered Pt–Co (fcc 1) (650 °C/7 h) with around 65.6 ± 2.4 wt.% exhibits a chemical composition from $Pt_{54}Co_{46}$ and a crystallite size of 1.8 ± 0.1 nm. Meanwhile, Pt–Co (fcc 1) (800 °C/7 h) exists up to 75.8 ± 1.9 wt.% with $Pt_{48}Co_{52}$ and a crystallite size of 2.2 ± 0.1 nm. For the Pt–Co sample (fcc 1) (900 °C/7 h), we obtained a disordered $Pt_{46}Co_{54}$ compound as major fraction with a crystallite size of 3.2 ± 0.1 nm. All Pt–Co samples reveal a minor fraction with a disordered Co rich alloy phase structure (fcc 2) and with a large crystallite size above 10 nm. The crystallite size was calculated from the complete XRD profile using the integral breadth method, which is independent of the distribution in size and shape of crystal domains. A volume average crystallite size is a determination of the size of a coherently diffraction domain. It should not be generally considered equivalent to the particle size, even though both are often used synonymously.

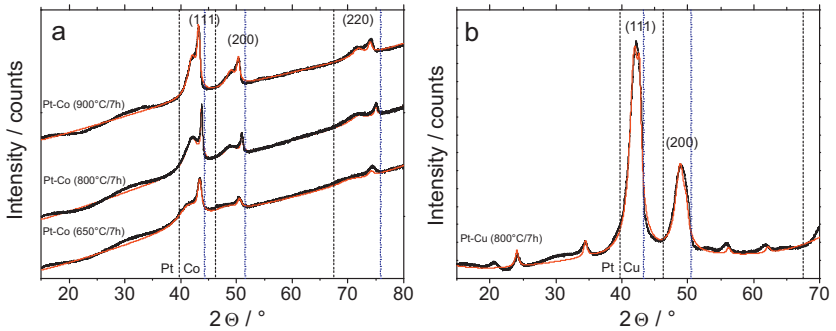

Fig. 1. XRD profiles of (a) synthesized Pt–Co catalysts, displayed with y-offset and (b) Pt–Cu alloy catalyst. Rietveld profile fit of diffraction data for Pt–Co (650 °C/7 h) (R_{wp} = 1.35, R_{exp} = 0.42, GOF = 3.18); for Pt–Co (800 °C/7 h) (R_{wp} = 1.51, R_{exp} = 0.41, GOF = 3.71); for Pt–Co (900 °C/7 h) (R_{wp} = 1.89, R_{exp} = 0.43, GOF = 4.38) and for Pt–Cu (800 °C/7 h) (R_{wp} = 2.77, R_{exp} = 0.60, GOF = 4.62). The fits are indicated by a red thin line. Vertical dotted lines denote Pt, Co and Cu reference patterns. PDF(Pt)#00-004-0802, PDF(Co)#00-015-0806, PDF(Cu)#00-004-0836. (For interpretation of the references to color in text, the reader is referred to the web version of the article.)

Table 1
Crystal structure, lattice parameter, crystallite size, Rietveld quantification and stoichiometric composition of Pt–Co and Pt–Cu alloy systems.

Catalyst	Crystal phase	Lattice parameter (Å)	Rietveld quantification (wt.%)	Crystallite size (nm)	Stoichiometric composition using Vegard's law
$PtCo_3$ (650 °C/7 h)	fcc 1	3.749 ± 0.001	65.6 ± 2.4	1.8 ± 0.1	$Pt_{54}Co_{46}$
	fcc 2	3.624 ± 0.001	34.4 ± 2.4	10.9 ± 0.9	$Pt_{21}Co_{79}$
$PtCo_3$ (800 °C/7 h)	fcc 1	3.726 ± 0.001	75.8 ± 1.9	2.2 ± 0.1	$Pt_{48}Co_{52}$
	fcc 2	3.585 ± 0.001	24.2 ± 1.9	17.5 ± 1.9	$Pt_{11}Co_{89}$
$PtCo_3$ (900 °C/7 h)	fcc 1	3.717 ± 0.001	62.0 ± 2.8	3.2 ± 0.1	$Pt_{46}Co_{54}$
	fcc 2	3.623 ± 0.001	38.0 ± 2.8	11.6 ± 1.1	$Pt_{21}Co_{79}$
$PtCu_3$ (800 °C/7 h)	fcc 1	3.705 ± 0.001	82.2 ± 2.0	3.6 ± 0.1	$Pt_{30}Cu_{70}$
	$L1_2$/fcc 2	3.641 ± 0.001	17.8 ± 2.0	10.3 ± 1.4	

The results of the main fraction for Pt–Co alloy system evidence that, that an increase in annealing temperature causes an increase in particle size at given annealing time; it does not cause additional Co insertion into the alloy and hence decrease of the alloy lattice parameter. Indeed, an increase of the annealing temperature only caused to a particle growth of Pt–Co alloy catalysts and very low decrease of the alloy lattice parameter by inserting of Co.

The XRD pattern of the composed $Pt_{35}Cu_{65}$ alloy catalyst, annealed at 800 °C for 7 h also reveals multiple crystal phase structures. The (1 1 1), (2 0 0) and (2 2 0) reflections occur between the pure Pt and Cu fcc crystal phases. It shifted to higher 2θ angles compared to those of pure Pt, indicated a contraction of the lattice and a Cu rich Pt alloy formation. The main fraction of the Pt–Cu sample exhibits a disordered fcc structure with Fm-3m space group. But, the additional small XRD peaks at around 24.1°, 34.3°, 55.7° and 61.5° recognize the coexistence of the ordered $PtCu_3$ alloy with Pm-3m $L1_2$/fcc 2 structure type. Here, Pt atoms are in the edges of the primitive cubic lattice and Cu atoms position all face centers. Referring to Table 1, the major fraction of the disordered $PtCu_3$ (fcc 1) crystal phase is around 82.2 ± 2.0 wt.% and for the ordered $L1_2$/fcc 2 Pt–Cu structure we establish around 17.8 ± 2.0 wt.%. Using Vegard's Law the disordered Pt–Cu alloy crystal phase as main compound is $Pt_{30}Cu_{70}$ with a crystallite size of 3.6 ± 0.1 nm.

3.2. Electrochemical dealloying of $PtCo_3$ and $PtCu_3$ alloy nanoparticle catalysts

The initial cyclic voltammograms (CV) obtained from the synthesis of nominal composed $Pt_{25}Co_{75}$ alloy nanoparticle catalysts, annealed at 650 °C, 800 °C and 900 °C for 7 h, are shown in Fig. 2. Pt–Co electrocatalysts reveal a similar electrochemical characteristic in the first CV profile. It is observed, that the initial CV exhibits a broad maximum current peak between 0.25 and 0.75 V/RHE during the anodic potential sweep, signifying the dissolution of the base metal Co on the surface of the Co rich Pt alloy nanoparticle. In addition, the voltammetric response displays the formation of the under potential deposited hydrogen (H_{upd}) in the potential range between 0.06 and 0.30 V/RHE, indicating also the presence of Pt atoms on the particle surface. The Co surface atoms do not participate in the H_{upd} regime. The hydrogen desorption regime overlaid partially with the dissolution current of Co in the first cycle. The observed CV profile infers that the segregation of Pt on the particle surface for Co rich Pt–Co alloy system was not reached by thermal treatment. The additional CVs also show that the Co dissolution continued slightly in a higher potential range between 0.50 and 0.80 V/RHE. The cathodic potential sweep exhibits any reduction of Co ions and their redeposition from the electrolyte on the particle surface of the Co rich Pt alloy electrocatalyst. It is quite evident that the large amount of Co lost in the first cycle. Further, the hydro-

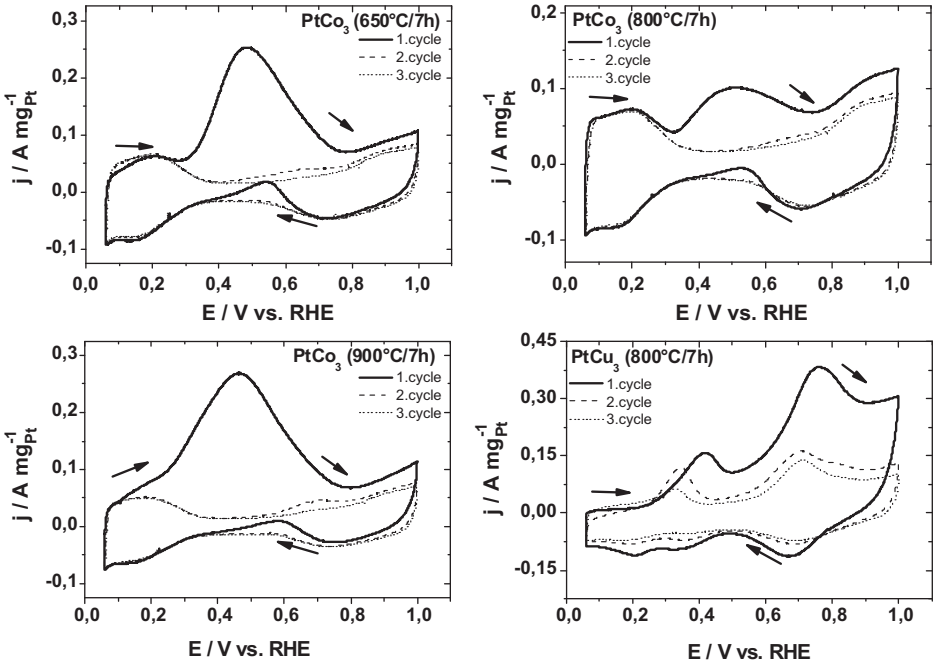

Fig. 2. Initial CV profiles of $PtCo_3$, annealed at 650 °C, 800 °C and 900 °C for 7 h and $PtCu_3$, annealed at 800 °C for 7 h. Cyclic voltammetry were conducted from 0.06 to 1.00 V/RHE with 100 mV s^{-1} in deaerated 0.1 M $HClO_4$ at room temperature.

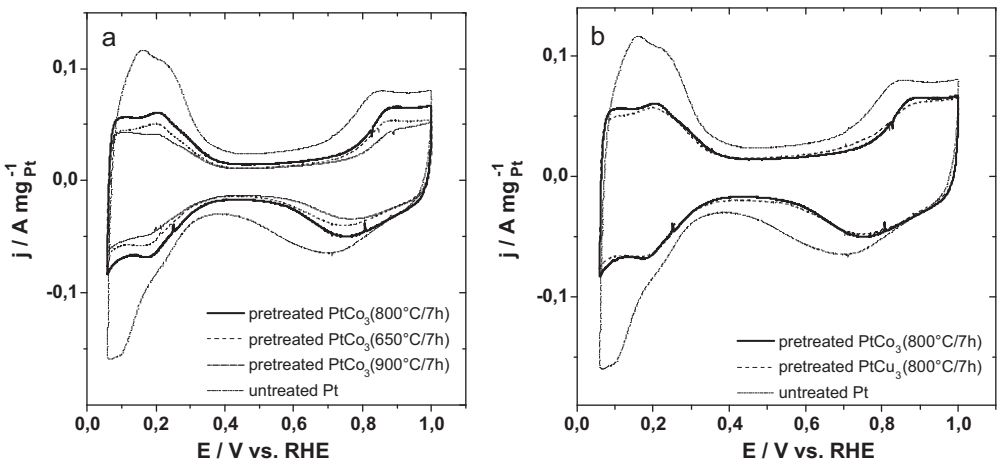

Fig. 3. (a) Final CV profiles of pretreated $PtCo_3$, annealed at 650 °C, 800 °C and 900 °C for 7 h compared with 28.2 wt.% Pt/HSAC. (b) Final CV profiles of pretreated $PtCo_3$ (800 °C/7 h) and pretreated $PtCu_3$ (800 °C/7 h) compared with 28.2 wt.% Pt/HSAC. Cyclic voltammetry were conducted from 0.06 to 1.00 V/RHE with 100 mV s^{-1} in deaerated 0.1 M $HClO_4$ at room temperature.

gen ad/desorption regime increased during the fast voltammetric cycling due to the enrichment and availability of Pt atoms on the particle surface.

Fig. 2 presents the initial CVs obtained from the $PtCu_3$ alloy nanoparticle catalyst, annealed at 800 °C for 7 h. It is noticed, that the first cycle shows no under potential deposited hydrogen (H_{upd}) regime between 0.06 and 0.30 V/RHE, indicating the absence of Pt atoms. It infers that the segregation and the enrichment of Cu atoms on surface was reached after thermal treatment. A participation of Cu surface atoms does not occur in the hydrogen ad/desorption regime. The voltammetric dissolution of Cu on the particle surface was observed in a broad potential range between 0.30 and 0.90 V/RHE during the anodic sweep in the first CV. The current peaks are around 0.34 V/RHE and 0.75 V/RHE. Referring to the peak positions, it is allowed to relate the different environments of Cu surface atoms in a Cu rich Pt alloy nanoparticle. The first peak at 0.34 V/RHE exhibits a Cu dissolution of pure, unalloyed Cu and corresponds to the standard Nernst potential. The second current peak at circa 0.75 V/RHE signifies the Cu stripping regime from a pure Pt and Pt rich alloy phases. The Cu dissolution on the surface of the alloy catalyst was further observed in the additional CVs. Here, the cathodic potential sweep shows an irreversible process of Cu dissolution. The dealloying process of a Cu rich Pt alloy nanoparticle catalyst was continued through 200 CV scans with 500 mV s^{-1} to dissolve quickly larger amount of Cu from the surface.

Fig. 3 presents the final CVs of electrochemical pretreated $PtCo_3$ (650 °C/7 h), $PtCo_3$ (800 °C/7 h), $PtCo_3$ (900 °C/7 h) and $PtCu_3$ (800 °C/7 h) electrocatalysts compared to that of a commercial 28.2 wt.% Pt/HSAC. It is clearly observed, that the final CV profile of each dealloyed electrocatalyst resembles a pure platinum CV, based on the covering of Pt atoms on the particle surface. In addition, the voltammetric pretreated $PtCo_3$ and $PtCu_3$ catalysts reveal an onset shift to higher potential around 0.80–0.90 V/RHE, which is to relate the activation of water and formation of oxygenated surface species on the Pt rich electrocatalyst surface. The anodic onset shift for Pt–Co and Pt–Cu catalysts about 50–60 mV indicates probably a reduction of the surface oxide coverage compared with pure Pt/C. A decrease in the surface coverage of platinum hydroxide and oxide may reflect a decrease in oxygen chemisorption energy on dealloyed surfaces and thus may result in activity enhancements. However, the voltammetric dissolution of the less noble metal may also result in an increase in surface roughness. The increase of the total particle surface area may also contribute in an increase in Pt mass based activities. Thus, the surface roughness may contribute to the improved activity for ORR.

Table 2 shows the comparison of the bulk composition of Pt–Co and Pt–Cu alloy electrocatalysts before and after voltammetric treatment. Again, it is noticed, that the initial EDS results are close to the nominal 25:75 atomic ratio of Pt:M (M = Co, Cu). The nominal chemical composition of Pt–Co alloy catalysts changed from initial $Pt_{28}Co_{72}$ (650 °C/7 h) to a final $Pt_{82}Co_{18}$, from initial $Pt_{37}Co_{63}$ (800 °C/7 h) to final $Pt_{80}Co_{20}$ and from initial $Pt_{27}Co_{73}$ (900 °C/7 h) to final $Pt_{73}Co_{27}$. It reveals that the Co loss of each Pt–Co catalyst is consistent with the observation in the voltammetric experiment. Meanwhile, the Pt–Cu alloy catalyst exhibits a Cu loss from the initial $Pt_{35}Cu_{65}$ (800 °C/7 h) to final $Pt_{65}Cu_{35}$ after the electrochemical dealloying and is in agreement with the observed voltammetric measurements. It is noted, that the Co concentration loss for $PtCo_3$ nanoparticles is higher using of the same electrochemical dealloying procedure than that for $PtCu_3$ catalyst.

3.3. ORR activity of dealloyed $PtCo_3$ and $PtCu_3$ alloy nanoparticle electrocatalysts

Fig. 4 shows the collected linear sweep voltammetric (LSV) profiles of dealloyed $PtCo_3$ and $PtCu_3$ alloy electrocatalysts for ORR obtained from the rotating disk electrode (RDE) experiments and compared with that for commercial 28.2 wt.% Pt/HSAC. It is observed, that each electrocatalyst exhibits a plateau behavior in the potential range between 0.06 and 0.70 V/RHE, indicating the diffusion-limited current regime. The diffusion-limited current regime displays that the diffusion of the reacting species to the electrocatalytic surface dominates over the reaction kinetic. For the pretreated $PtCo_3$ (650 °C/7 h), $PtCo_3$ (800 °C/7 h), $PtCo_3$ (900 °C/7 h), $PtCu_3$ (800 °C/7 h), and untreated Pt/HSAC, the diffusion-limited current density is in range between −5 and −6 mA cm_{geo}^{-2}. The onset potential of each Pt–Co and Pt–Cu alloy catalyst from a mixed kinetic-diffusion control to a diffusion-limiting region followed at around 0.70 V/RHE. It is quite evident, that the open circuit potential for dealloyed Pt–Co and Pt–Cu alloy catalysts is around 1.02 V/RHE and shifts to higher potential compared to 28.2 wt.% Pt/HSAC at 0.99 V/RHE. The significant onset shift reveals the enhanced activity, approaching to the thermodynamic value for ORR. Here, the mixed region of pretreated alloy catalysts moves to more positive potentials compared to that for pure Pt/HSAC. Note, the potential shift is about 50 mV and is in the potential range with the delayed onset of the oxide formation, observed from the final CV during the anodic sweep. Pt-mass based and ECSA-based specific activities of each electrocatalyst were established at 0.90 V/RHE

Table 2
Comparison of chemical composition before and after voltammetric treatment and catalytic activities of $PtCo_3$, $PtCu_3$ alloy and Pt/HSAC catalysts for ORR.

Catalyst	Chemical composition via EDS (at.%)	Chemical composition final via EDS (at.%)	Electrochemical surface area (ECSA) ($m^2\ g_{Pt}^{-1}$)	Specific current density at 0.90 V/RHE ($\mu A\ cm_{Pt}^{-2}$)	Pt mass based current density at 0.90 V/RHE ($A\ mg_{Pt}^{-1}$)	Tafel slope for low current density region (lcd) ($mV\ dec^{-1}$)
$PtCo_3$ (650 °C/7 h)	$Pt_{28}Co_{72}$	$Pt_{82}Co_{18}$	40 ± 4	701 ± 68	0.28 ± 0.05	75
$PtCo_3$ (800 °C/7 h)	$Pt_{37}Co_{63}$	$Pt_{80}Co_{20}$	45 ± 4	804 ± 146	0.38 ± 0.05	80
$PtCo_3$ (900 °C/7 h)	$Pt_{27}Co_{73}$	$Pt_{73}Co_{27}$	36 ± 2	811 ± 99	0.29 ± 0.04	85
$PtCu_3$ (800 °C/7 h)	$Pt_{35}Cu_{65}$	$Pt_{65}Cu_{35}$	47 ± 2	873 ± 167	0.41 ± 0.09	65
Pt/HSAC	Pt_{100}	Pt_{100}	73 ± 3	179 ± 4	0.13 ± 0.01	61

at room temperature and corrected for mass transport limitation, respectively.

Fig. 5 presents the normalized ECSA-based and Pt-mass based Tafel plots, obtained from the kinetic current j_{kin} for pretreated $PtCo_3$ and $PtCu_3$ catalysts and compared to those for 28.2 wt.% Pt/HSAC. The Tafel plots reveal the considerable improvement of intrinsic activities for all Pt–Co and Pt–Cu alloy catalysts. It is to see, that the Tafel slope for ORR changes continuously in the examined potential range. The experimental data exhibits two Tafel slopes at low current density (lcd) and high current density (hcd) region and compared to those from the literature. The results of the Tafel slope for the low current region are only summarized in Table 2. The previously reported values of the Tafel slope for a single crystal Pt [33], polycrystalline Pt and carbon supported Pt nanoparticle [34] are around −2.3 RT/F at low overpotentials ($E > 0.85$ V/RHE) and -2×2.3 RT/F ($E < 0.85$ V/RHE) at high overpotentials. The values of the Tafel slope for all pretreated $PtCo_3$ electrocatalysts at the low current density (lcd) region are slightly higher compared to the experimental value for Pt nanoparticles and to the Tafel slope of 60 $mV\ dec^{-1}$ for bulk and single Pt crystals from the cited literature data. But, the Tafel slopes at the high current density region for $PtCo_3$ samples are clearly higher than that obtained from Pt nanoparticles and literature references. It is noted, that Tafel slopes at lcd and hcd region for pretreated $PtCu_3$ agreed well with the above cited literature data. Gasteiger et al. and Paulus et al. explained that the difference of the Tafel slope can be attributed with the change of oxide species adsorption on the Pt–Co alloy surface [2,4].

Table 2 presents the ECSA, Pt-mass based and the ECSA-based specific activities of pretreated $PtCo_3$ (650 °C/7 h), $PtCo_3$ (800 °C/7 h), $PtCo_3$ (900 °C/7 h) and $PtCu_3$ (800 °C/7 h) alloy nanoparticle electrocatalysts compared to a commercial carbon supported Pt catalyst. It is clearly observed, that the ECSA of electrochemical pretreated Pt–Co and Pt–Cu samples is smaller than that for supported Pt. The reduced ECSA values only caused to an increase of the particle size through the thermal treatment for the alloy formation. However, after the voltammetric dealloying of $PtCo_3$ and $PtCu_3$ the surface area increased through the surface roughness. However, the effect of the surface roughness cannot explain alone the reduced ECSA values and simultaneously the significantly enhanced ORR activity of dealloyed Pt–Co and Pt–Cu electrocatalysts. Referring to Fig. 5 and Table 2, the Pt-mass and surface area specific ORR activities of Pt–Co and Pt–Cu alloy electrocatalysts after voltammetric activation by dealloying exhibit a considerable improvement compared to those of pure Pt/C. The dealloyed $PtCo_3$ (800 °C/7 h) electrocatalyst shows 3 times higher in terms of Pt-based mass activity and 4–5 times higher in terms of ECSA-based specific activity than a 28.2 wt.% Pt/HSAC. Meanwhile, $PtCo_3$ (650 °C/7 h) and $PtCo_3$ (900 °C/7 h) display two folds for the mass activity increase compared to Pt/HSAC. This observation indicates that an increase of the annealing temperature affected no mass activity benefit. Generally, the surface area specific activity of Pt–Co electrocatalysts increases with the particle size. Thereby, $PtCo_3$ (650 °C/7 h) with a particle size of 1.8 ± 0.1 nm had the smallest and $PtCo_3$ (900 °C/7 h) with 3.2 ± 0.1 nm the highest value of the specific activity. Dealloyed Pt–Co catalysts, annealed at 800 °C showed the most favorable balance between mass and specific ORR activity with a particle size of 2.2 ± 0.1 nm. Dealloyed $PtCu_3$ (800 °C/7 h) exhibited a 3–4 fold increase in mass activity and 5–6 fold increase in specific activity compared to pure Pt. Thus, dealloyed $PtCu_3$ is still the most active ORR catalyst. But, the surface area specific activity of dealloyed $PtCu_3$ is similar to that of $PtCo_3$ (800 °C/7 h). The increasing improvement for ORR activity can be attributed with the uniformity of the Pt–Co crystal phase at various annealing temperatures. The disordered fcc crystal phase structure of $PtCo_3$ (800 °C/7 h) (fcc 1) exists up to 75.8 ± 1.9 wt.% and is more

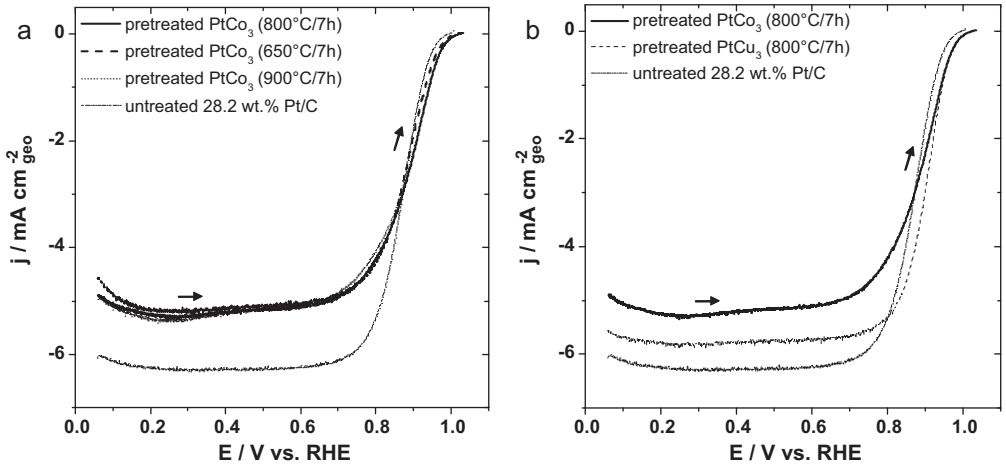

Fig. 4. (a) LSV profiles of pretreated $PtCo_3$/HSAC, annealed at 650 °C, 800 °C and 900 °C for 7 h compared with 28.2 wt.% Pt/HSAC for ORR. Pt loading of the Pt–Co system is in a range between 11 and 12 $\mu g\ cm_{geo}^{-2}$. (b) LSV profiles of pretreated $PtCo_3$/HSAC (800 °C/7 h) and $PtCu_3$/HSAC (800 °C/7 h) with 11.5 $\mu g\ Pt\ cm_{geo}^{-2}$ for ORR compared to pure 28.2 wt.% Pt/HSAC with 14.6 $\mu g\ Pt\ cm_{geo}^{-2}$. Linear sweep voltammetry were conducted anodically from 0.06 to 1.05 V/RHE with 5 $mV\ s^{-1}$ and 1600 rpm in oxygen saturated 0.1 M $HClO_4$ at room temperature.

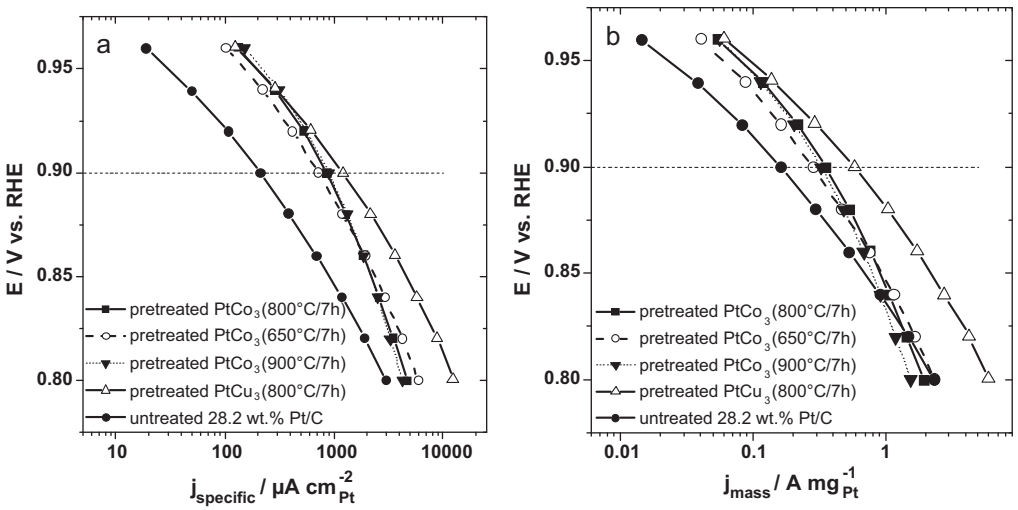

Fig. 5. (a) Pt ECSA-based Tafel plots of pretreated $PtCo_3$/HSAC, annealed at 650 °C, 800 °C and 900 °C for 7 h and pretreated $PtCu_3$/HSAC (800 °C/7 h) compared with pure 28.2 wt.% Pt/HSAC. (b) Pt mass-based Tafel plots of pretreated $PtCo_3$/HSAC, annealed at 650 °C, 800 °C and 900 °C for 7 h and pretreated $PtCu_3$/HSAC (800 °C/7 h) compared with pure 28.2 wt.% Pt/HSAC.

uniform than $PtCo_3$ (650 °C/7 h) and $PtCo_3$ (900 °C/7 h). The Pt–Co system with multiple alloy phase structures does not display a very active class of electrocatalysts. The increase of the uniformity of single-phase alloy leads to an improved ORR activity for the Co rich Pt–Co system.

3.4. ORR selectivity of dealloyed $PtCo_3$ and $PtCu_3$ alloy nanoparticles

For further studies, we established in a RRDE measurement the number of transfer electrons and the percentage of the hydrogen peroxide production during oxygen reduction reaction on the active surface of dealloyed $PtCo_3$ (800 °C/7 h) and $PtCu_3$ (800 °C/7 h) as the most active catalysts. The RRDE experiment was conducted in oxygen saturated 0.1 M $HClO_4$ at room temperature. Fig. 6 shows the polarization curves at various rotating speeds, the inserted Koutecki–Levich plot and the collected ring current of H_2O_2 oxidation obtained during the LSV measurements of dealloyed $PtCo_3$ (800 °C/7 h) and $PtCu_3$ (800 °C/7 h) electrocatalysts at 1600 rpm. The LSV experiment of the disk electrode prepared with a thin catalyst film exhibits nearly a well-defined diffusion limiting current for ORR (0.2–0.7 V/RHE) followed by a mixed kinetic diffusion control regime between 0.8 and 1.0 V/RHE. It is clearly observed, that the simultaneously recorded ring current (i_{ring}) (at 1600 rpm) for the oxidation of the generated H_2O_2 is only a small fraction of the disk current (i_{disk}) in all potential regimes. The ring current decreased gradually during the anodical sweep of the disk electrode for pretreated $PtCo_3$ (800 °C/7 h) and $PtCu_3$ (800 °C/7 h) and was close to zero at the kinetic diffusion regime. The evidence is that ORR proceeds exclusively through a four electron reduction pathway. Here, the ring measurements of peroxide oxidation were recorded by different rotating speeds and were independent from the measured speed range. The influence of the H_2O_2 production on the bare, highly polished and cleaned glassy carbon electrode is also negligible.

The ring current is related to the disk current by a quantity N, the collection efficiency.

$$N = -\frac{i_{ring}}{i_{disk}} \quad (1)$$

The collection efficiency of the ring disk electrode was previously measured in a simple Fe^{2+}/Fe^{3+} redox reaction system in a RRDE setup, respectively [35]. It persists unchanged at $N = 0.16 \pm 0.02$ for a wide range of the rotating speed.

The quantification of the peroxide production was calculated from [36]

$$X_{H_2O_2} = \frac{2 \times (i_{ring}/N)}{(i_{disk} + (i_{ring}/N))} \quad (2)$$

Fig. 7 presents the hydrogen peroxide production with the disk potential during the oxygen reduction for dealloyed $PtCo_3$ (800 °C/7 h) and $PtCu_3$ (800 °C/7 h) and compared to that for untreated 28.2 wt.% Pt/HSAC. The peroxide production was calculated from the data in Fig. 6 at 1600 rpm using the equation (2) with $N = 0.16 \pm 0.02$. The platinum loading of $PtCo_3$ and $PtCu_3$ catalysts was around 11 $\mu g\,cm_{geo}^{-2}$ and for Pt/HSAC it was 15 $\mu g\,cm_{geo}^{-2}$. Again, it is clearly noticed, that the peroxide fraction is under 0.5% up to 0.20 V/RHE, indicating, that the reduction of O_2 runs exclusively via a direct four electron step in the potential relevant to the fuel cell cathodes. The RRDE study reveals that the peroxide production decreases continuously with higher disk potential for dealloyed Pt–Co and Pt–Cu and shows the highest values in the H_{upd} regime between 0.06 and 0.30 V/RHE. Indeed, the slightly enhanced coadsorption of H_2O_2 in the H_{upd} region blocks the dissociation of molecularly adsorbed hydrogen. The peroxide production of dealloyed $PtCo_3$ (800 °C/7 h) is slightly higher than that for dealloyed $PtCu_3$ (800 °C/7 h) with similar Pt loading. The enhanced H_2O_2 production during the ORR is probably attributed to the particle size effect. Durand and co-workers [37–39], Hanson and Boudart [40] and Hwang and Chung [41] reported that the degree of surface coverage by oxygenated species increases with the decrease of the particle size. From the XRD results the particle size for $PtCo_3$ (800 °C/7 h) is smaller than that for $PtCu_3$ (800 °C/7 h). It is evident, that the H_2O_2 production increases, when the particle size decreases and is consistent to previously reported literature. Meanwhile, the commercial 28.2 wt.% Pt/HSAC exhibits the lowest H_2O_2 production. Here, the platinum loading is higher than those for Pt alloy catalysts. Indeed, the peroxide production increased with the decrease of the platinum loading and is consistent with the reports from Inaba et al. [42] and Bonakdarpour et al. [43]. But, the high surface area carbon (HSAC) support has also a considerable influence on the H_2O_2 production. The oxygen reduction on carbon only occurs at low potentials and causes to an increase of the amount of H_2O_2 species. Referring to Fig. 7, the untreated

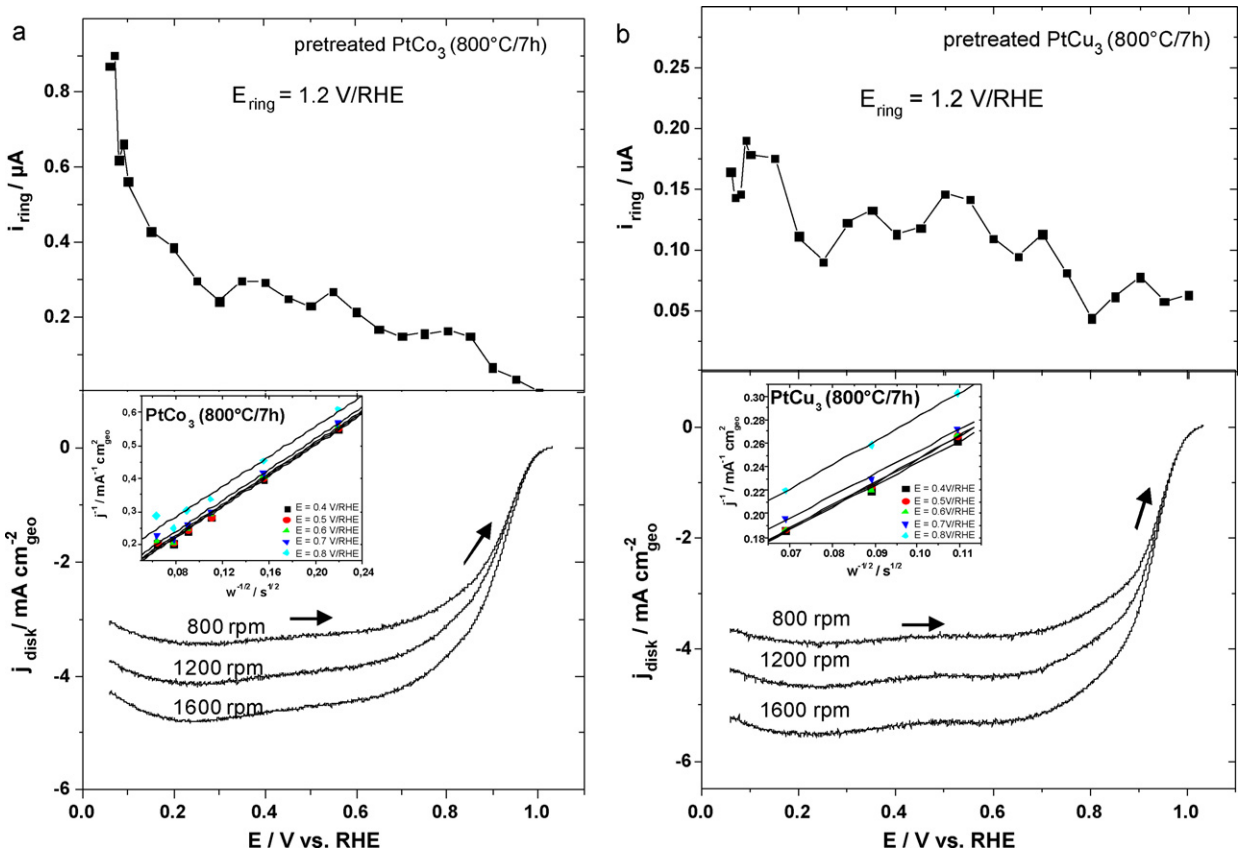

Fig. 6. RRDE measurements of the oxygen reduction reactivity for (a) Pt–Co and (b) Pt–Cu catalysts. Insert: Koutecki–Levich plots of dealloyed $PtCo_3$ (800 °C/7 h) and $PtCu_3$ (800 °C/7 h) at various electrode potentials. Linear sweep voltammetry were conducted anodically from 0.06 to 1.05 V/RHE with 5 mV s^{-1} in oxygenated 0.1 M $HClO_4$ at room temperature. Simultaneously recorded ring current at 1600 rpm for a ring potential of E_{ring} = 1.20 V/RHE.

pure HSAC with a loading of around 51.0 µg cm_{geo}^{-2} exhibits a H_2O_2 production above 10% in a potential range between 0.06 and 0.25 V/RHE. The modification and activity change of HSAC was not examined after the thermal treatment. Hence, we assumed that the influence on H_2O_2 production from carbon is stronger at the low potentials than the particle size effect and the Pt loading effect. In summary, the H_2O_2 production for dealloyed $PtCu_3$ (800 °C/7 h) and pure Pt nanoparticle catalysts is negligible based on the small produced fraction below 0.5% during the ORR. The H_2O_2 production for dealloyed $PtCo_3$ (800 °C/7 h) decreased further below 0.5% above 0.20 V/RHE. It is evident, that the direct four electron transfer is the main mechanism for oxygen reduction on dealloyed $PtCo_3$, $PtCu_3$ and Pt nanoparticle electrocatalysts.

In Fig. 6, the Koutecki–Levich plots for pretreated $PtCo_3$ (800 °C/7 h) and $PtCu_3$ (800 °C/7 h) reveal a proportional dependence of the limiting current on the square root of the rotation rate in oxygen saturated 0.1 M $HClO_4$ at room temperature. The plot of $1/j$ vs. $\omega^{-1/2}$ is linear and the fits run nearly parallel at various electrode potentials, indicating a similar slope. The intercepts of $1/j$ axis at $1/\omega^{1/2} = 0$ gives the magnitude of the absolute kinetic current for that process in the absence of any mass transfer effects. From the slope of Koutecki–Levich plots, so-called "*B* factor", it can be calculated the number of transfer electrons in the reduction of oxygen molecule and proved with the theoretical value for a four electron pathway. The Koutecki–Levich equation is described as follows

$$\frac{1}{j} = \frac{1}{j_{kin}} + \frac{1}{j_{dif}} = \frac{1}{j_{kin}} + \frac{1}{(B \times w^{1/2})} \quad (3)$$

$$B = 0.62 \times n \times F \times D(O_2)^{2/3} \times \nu^{-1/6} \times c(O_2) \quad (4)$$

where j_{kin} is the kinetic current density, j_{dif} is the diffusion-limiting current density through the solution boundary layer, *B* is a constant, ω is the rotation rate and *F* is Faraday constant (F = 96485 C mol^{-1}). The theoretical value for *B* is calculated for four electron reduction process using published data for the oxygen diffusivity ($D(O_2) = 1.93 \times 10^{-5}$ cm^2 s^{-1}) [44], the

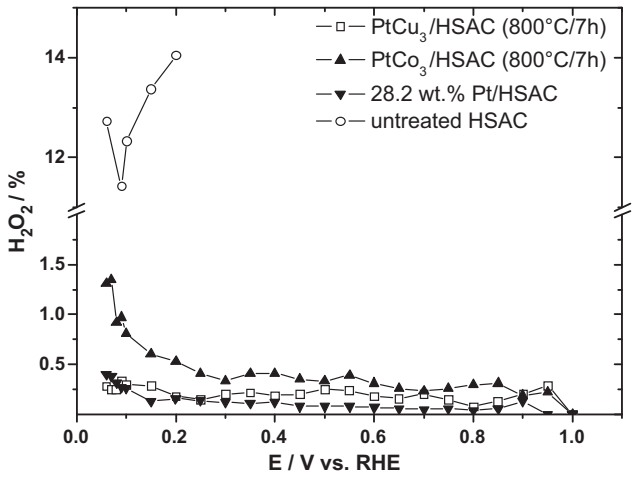

Fig. 7. Hydrogen peroxide production with the disk potential during the O_2 reduction on pretreated $PtCo_3$/HSAC (800 °C/7 h) with Pt loading 11.4 µg cm_{geo}^{-2}, pretreated $PtCu_3$/HSAC (800 °C/7 h) with Pt loading 11.4 µg cm_{geo}^{-2}, untreated 28.2 wt.% Pt/HSAC with Pt loading 14.6 µg cm_{geo}^{-2} and untreated pure HSAC with carbon loading 51.0 µg cm_{geo}^{-2} in oxygen saturated 0.1 M $HClO_4$ at room temperature. Calculated from the data in Fig. 6 (at 1600 rpm) using Eq. (2) with $N = 0.16 \pm 0.02$.

kinematic viscosity of the electrolyte ($\nu = 1.009 \times 10^{-2}\,cm^2\,s^{-1}$) [44] and O_2 solubility ($c(O_2) = 1.26 \times 10^{-3}\,mol\,l^{-1}$) [45]. We obtained for dealloyed $PtCo_3$ (800 °C/7 h) an experimental value of $B = 0.429 \pm 0.005\,mA\,cm_{geo}^{-2}\,s^{1/2}$ and is in agreement with the theoretical value of $B = 0.467\,mA\,cm_{geo}^{-2}\,s^{1/2}$ for a four electron reduction. For dealloyed $PtCu_3$ (800 °C/7 h) the resulting value of $B = 0.494 \pm 0.007\,mA\,cm_{geo}^{-2}\,s^{1/2}$ is also consistent. Here, the current of peroxide oxidation on the Pt ring is negligible due to the previously demonstrated results from the RRDE experiment.

In summary, RRDE and RDE experiments for dealloyed $PtCo_3$ (800 °C/7 h) and $PtCu_3$ (800 °C/7 h) reveal a four electron reduction pathway in a proton exchange membrane fuel cell. Again, the effect of surface roughness cannot explain alone the significantly enhanced Pt mass based and specific activities of Pt–Co and Pt–Cu catalysts after initial voltammetric activation. We did not have a fundamental understanding of the mechanism for ORR at an atomic scale for the Pt–Co system. Our hypothesis is, that geometric strain effects of the dealloyed Pt–Co nanoparticles, similar to those found out for dealloyed $PtCu_3$ nanoparticles, are responsible for the improvement in ORR activity [1]. In the case of dealloyed $PtCu_3$, we demonstrated a compressive lattice strain in the Pt shell of a core shell particle. It was provided an activity–strain relationship for the better understanding of the enhanced improvement of dealloyed Cu rich Pt alloy nanoparticle. For $PtCo_3$ system we are currently preparing the DFT calculation to prove the geometric effect. More details are necessary and in preparation to clarify the enhanced activity and structural modification of dealloyed Pt–Co system.

4. Conclusion

This work demonstrated a comparative synthesis, structural characterization, electrochemical measurements and ORR activity of $PtCo_3$ alloy nanoparticle electrocatalysts, annealed at various temperatures and compared with $PtCu_3$ alloy catalyst and commercial Pt/HSAC. The variation of the annealing temperature for the alloy formation of the Pt–Co system was correlated with crystal phase structure, chemical composition, particle size, ECSA, mass and surface area specific activity for ORR.

- The actual chemical composition via EDS was close to an atomic ratio from 25 at.% Pt:75 at.% Co/Cu for each alloy electrocatalyst. The XRD results correlated with Vegard's Law, in contrast, revealed that the disordered fcc $Pt_{50}Co_{50}$ (Fm-3m) with small particle size (2–3 nm) is the main compound for the Pt–Co system, annealed at various temperatures.
- The increase of the annealing temperature only causes to a particle growth but very low insertion of Co in the Pt lattice for alloy formation.
- Dealloyed $PtCo_3$ catalysts, annealed at 800 °C for 7 h showed the most favorable balance between mass and specific ORR activity with a particle size of 2.2 ± 0.1 nm compared with $PtCo_3$ (650 °C/7 h) and $PtCo_3$ (900 °C/7 h). $PtCo_3$ (800 °C/7 h) exhibited 3 times higher in terms of mass activity and 4–5 times higher in terms of specific activity after the voltammetric activation by dealloying than 28.2 wt.% Pt/HSAC.
- The increasing improvement can be related to the uniformity of Pt–Co crystal phase.
- Dealloyed $PtCu_3$ is still the most active catalyst for ORR than dealloyed $PtCo_3$.
- The hydrogen peroxide production is very low for dealloyed $PtCo_3$ (800 °C/7 h) and $PtCu_3$ (800 °C/7 h). RRDE and RDE experiments revealed for these electrocatalysts a four electron reduction pathway in a proton exchange membrane fuel cell.

Acknowledgements

The authors would like to thank Dipl.-Chem. Frédéric Hasché, Annette Wittebrock and Dr. Elisabeth Irran for laboratory support and in particular the Department of the Electron Microscopy at the Technical University of Berlin. This project was supported by the DFG-funded Cluster of Excellence "Unifying Concepts in Catalysis" (UniCat) at the Technical University of Berlin, Germany.

References

[1] P. Strasser, S. Koh, T. Anniyev, J. Greeley, K. More, C. Yu, Z. Liu, S. Kaya, D. Nordlund, H. Ogasawara, M.F. Toney, A. Nilsson, Nat. Chem. 2 (2010) 454–460.
[2] H.A. Gasteiger, S.S. Kocha, B. Sompalli, F.T. Wagner, Appl. Catal. B: Environ. 56 (2005) 9–35.
[3] T. Toda, H. Igarashi, H. Uchida, M. Watanabe, J. Electrochem. Soc. 146 (1999) 3751.
[4] U.A. Paulus, A. Wokaun, G.G. Scherer, T.J. Schmidt, V. Stamenkovic, V. Radmilovic, N.M. Markovic, P.N. Ross, J. Phys. Chem. B 106 (2002) 4181–4191.
[5] U.A. Paulus, T.J. Schmidt, H.A. Gasteiger, R.J. Behm, J. Electroanal. Chem. 495 (2001) 134–145.
[6] V. Stamenkovic, B.S. Mun, M. Arenz, K.J.J. Mayerhofer, C.A. Lucas, G. Wang, P.N. Ross, N. Markovic, Nat. Mater. 6 (2007) 241.
[7] S. Koh, N. Hahn, C. Yu, P. Strasser, J. Electrochem. Soc. 155 (2008) B1281–1288.
[8] S. Chen, H.A. Gasteiger, K. Hayakawa, T. Tada, Y. Shao-Horn, J. Electrochem. Soc. 157 (2010) A82–A97.
[9] S. Koh, P. Strasser, J. Am. Chem. Soc. 129 (2007) 12624–12625.
[10] S. Ratndeep, M. Prasanna, H. Nathan, S. Peter, Angew. Chem. Int. Ed. 46 (2007) 8988–8991.
[11] Z. Liu, S. Koh, C. Yu, P. Strasser, J. Electrochem. Soc. 154 (2007) B1192–B1199.
[12] V.R. Stamenkovic, B.S. Mun, K.J.J. Mayrhofer, P.N. Ross, N.M. Markovic, J. Am. Chem. Soc. 128 (2006) 8702–8988.
[13] V. Stamenkovicĭ, T.J. Schmidt, P.N. Ross, N.M. Markovic, J. Phys. Chem. B 106 (2002) 11970–11979.
[14] R.R. Adzic, J. Zhang, K. Sasaki, M.B. Vukmirovic, M. Shao, J.X. Wang, A.U. Nilekar, M. Mavrikakis, J.A. Valerio, F. Uribe, Top. Catal. 46 (2007) 249–262.
[15] M. Watanabe, K. Tsurumi, T. Mizukami, T. Nakamura, P. Stonehart, J. Electrochem. Soc. 141 (1994) 2659–2668.
[16] K.J.J. Mayrhofer, K. Hartl, V. Juhart, M. Arenz, J. Am. Chem. Soc. 131 (2009) 16348–16349.
[17] J. Zhang, Y. Mo, M.B. Vukmirovic, R. Klie, K. Sasaki, R.R. Adzic, J. Phys. Chem. B 108 (2004) 10955–10964.
[18] J. Zhang, Y. Mo, M. Vukmirovic, R. Klie, K. Sasaki, R. Adzic, J. Phys. Chem. B 108 (2004) 10955–10964.
[19] M.H. Lee, J.S. Do, J. Power Sources 188 (2009) 353–358.
[20] S. Koh, M.F. Toney, P. Strasser, Electrochim. Acta 52 (2007) 2765–2774.
[21] J.R.C. Salgado, E. Antolini, E.R. Gonzalez, J. Power Sources 141 (2005) 13–18.
[22] V. Stamenkovic, T.J. Schmidt, P.N. Ross, N.M. Markovic, J. Phys. Chem. B 106 (2002) 11970–11979.
[23] S. Koh, J. Leisch, M.F. Toney, P. Strasser, J. Phys. Chem. C 111 (2007) 3744–3752.
[24] S. Chen, W. Sheng, N. Yabuuchi, P.J. Ferreira, L.F. Allard, Y. Shao-Horn, J. Phys. Chem. C 113 (2008) 1109–1125.
[25] F.H.B. Lima, J.F.R. de Castro, L.G.R.A. Santos, E.A. Ticianelli, J. Power Sources 190 (2009) 293–300.
[26] F.J. Lai, W.N. Su, L. Sarma, D.G. Liu, C.A. Hsieh, J.F. Lee, B.J. Hwang, Chem. Eur. J. 16 (2010) 4602–4611.
[27] C. Wang, D. van der Vliet, K.-C. Chang, H. You, D. Strmcnik, J.A. Schlueter, N.M. Markovic, V.R. Stamenkovic, J. Phys. Chem. C 113 (2009) 19365–19368.
[28] H. Schulenburg, E. Müller, G. Khelashvili, T. Roser, H. Bönnemann, A. Wokaun, G.G. Scherer, J. Phys. Chem. C 113 (2009) 4069–4077.
[29] H. Schulenburg, J. Durst, E. Müller, A. Wokaun, G.G. Scherer, J. Electroanal. Chem. 642 (2010) 52–60.
[30] M. Oezaslan, F. Hasche, P. Strasser, ECS Trans. 33 (2010) 333–341.
[31] H.A. Gasteiger, N.M. Markovi, Science 324 (2009) 48–49.
[32] P. Mani, R. Srivastava, P. Strasser, J. Power Sources 196 (2011) 666–673.
[33] B.N. Grgur, N.M. Markovic, P.N. Ross, Can. J. Chem. 75 (1997) 1465–1471.
[34] T.J. Schmidt, U.A. Paulus, H.A. Gasteiger, R.J. Behm, J. Electroanal. Chem. 508 (2001) 41–47.
[35] T.J. Schmidt, H.A. Gasteiger, in: W. Vielstich, A. Lamm, H. Gasteiger (Eds.), Handbook of Fuel Cells—Fundamentals, Technology, and Applications, Wiley, Chichester, 2006, p. 316 (Chapter 322).
[36] N.M. Markovic, H.A. Gasteiger, J. Philip, N. Ross, J. Phys. Chem. 99 (1995) 3411–3415.
[37] A. Kabbabi, F. Gloaguen, F. Andolfatto, R. Durand, J. Electroanal. Chem. 373 (1994) 251–254.
[38] A. Gamez, D. Richard, P. Gallezot, F. Gloaguen, R. Faure, R. Durand, Electrochim. Acta 41 (1996) 307–314.
[39] O. Antoine, R. Durand, J. Appl. Electrochem. 30 (2000) 839–844.
[40] F.V. Hanson, M. Boudart, J. Catal. 53 (1978) 56–67.
[41] J.T. Tae Hwang, J.S. Chung, Electrochim. Acta 38 (1993) 2715–2723.

[42] M. Inaba, H. Yamada, J. Tokunaga, A. Tasaka, Electrochem. Solid-State Lett. 7 (2004) A474–A476.
[43] A. Bonakdarpour, T.R. Dahn, R.T. Atanasoski, M.K. Debe, J.R. Dahn, Electrochem. Solid-State Lett. 11 (2008) B208–B211.
[44] N.M. Markovic, H.A. Gasteiger, B.N. Grgur, P.N. Ross, J. Electroanal. Chem. 467 (1999) 157–163.
[45] CRC Handbook of Chemistry and Physics, CRC Press, New York, 1996.